EUROFUSION WPJET1-PR(16) 14447

L Frassinetti et al.

Global and pedestal confinement and pedestal structure in dimensionless collisionality scans of low triangularity H-mode plasmas in JET-ILW

Preprint of Paper to be submitted for publication in
Nuclear Fusion

This work has been carried out within the framework of the EUROfusion Consortium and has received funding from the Euratom research and training programme 2014-2018 under grant agreement No 633053. The views and opinions expressed herein do not necessarily reflect those of the European Commission.

Global and pedestal confinement and pedestal structure in dimensionless collisionality scans of low triangularity H-mode plasmas in JET-ILW

L. Frassinetti[1], M. N. A. Beurskens[2,3], S. Saarelma[3], J. E. Boom[4], E. Delabie[5], J. Flanagan[3], M. Kempenaars[3], C. Giroud[3], P. Lomas[3], L. Meneses[6], C.S. Maggi[3],S. Menmuir[3], I. Nunes[6], F. Rimini[3], E. Stefanikova[1], H. Urano[7] , G. Verdoolaege[8,9] and JET contributors*

EUROfusion Consortium, JET, Culham Science Centre, Abingdon, OX14 3DB, UK

[1]Division of Fusion Plasma Physics, KTH Royal Institute of Technology, Stockholm SE

[2]Max-Planck-Institut für Plasmaphysik, D-17491 Greifswald, Germany

[3]CCFE, Culham Science Centre, Abingdon,OX14 3DB, UK

[4]Max-Planck-Institut für Plasma Physik, Boltzmannstr.2, 85748 Garching, Germany

[5]Oak Ridge National Laboratory, Oak Ridge, TN 37831-6169 USA

[6]Instituto de Plasmas e Fusão Nuclear, IST, Universidade de Lisboa, 1049-001 Lisboa, Portugal

[7]Japan Atomic Energy Agency, Naka Fusion Institute, Naka, 311-0193, Japan

[8]Department of Applied Physics Ghent University Sint-Pietersnieuwstraat 41 B-9000 Ghent, Belgium

[9]Laboratory for Plasma Physics—Royal Military Academy (LPP-ERM/KMS), Avenue de la Renaissancelaan 30, B-1000 Brussels, Belgium

** See the Appendix of F. Romanelli et al., Proceedings of the 25th IAEA Fusion Energy Conference 2014, Saint Petersburg, Russia*

Abstract

A dimensionless collisionality scan in low triangularity plasmas in the Joint European Torus with the ITER-like wall (JET-ILW) has been performed. The increase of the confinement with decreasing collisionality is observed. At low collisionality, a confinement factor comparable to JET-C is achieved. At high collisionality, the low confinement is related to a degraded pedestal temperature.

The increase of confinement with decreasing collisionality is due to both the increase in the pedestal and in the core pressure. The improvement in the pedestal is related only to the temperature increase. The improvement in the core is stronger and is driven by (i) the core temperature increase via the temperature profile stiffness and by (ii) the density peaking increase driven by the low collisionality.

The EPED1 model predictions show a reasonable qualitative agreement with experimental results in terms of the scaling of pedestal pressure height with collisionality. From a quantitative point of view, the disagreement increases at high collisionality. In terms of the pedestal width, the kinetic ballooning mode (KBM) constraint and the experimental data are in good agreement only at low collisionality. The experimental pedestal width increases with collisionality. Nonetheless, an extrapolation to low collisionality values suggests that the width predictions from the KBM constraint are reasonable for ITER.

The stability analysis performed with the ELITE code has a reasonable qualitative agreement with the experimental pedestal results. The operational points are in the stable region both at low and high collisionality considering the *n=70* boundary. The behaviour of the stability boundary and α_{max} show the improvement of the pedestal stability at low collisionality, in agreement with the experimental observations.

1. INTRODUCTION

The baseline type I ELMy H-mode scenario has been re-established in JET with the new tungsten divertor and beryllium main wall (JET-ILW) in 2011 [Brezinsek 2012, Matthews 2012]. The initial results have shown a confinement degradation of the ITER baseline scenarios with a confinement factor in the range H_{98}≈0.8-0.9 [Giroud NF2013, Beurskens NF2014] compared to H_{98}≈1.0 in the carbon wall JET (JET-C). This has been attributed, at least in part, to the achievable operational space obtained in the initial JET-ILW campaigns that was restricted to high plasma density to reduce W accumulation in the core [Beurskens NF2014, Nunes IAEA 2014, Nunes EPS2015]. The degraded confinement was mainly driven by a lower pedestal pressure due to a pedestal temperature approximately 20-30% lower than in JET-C. Moreover, while JET-C has achieved a better confinement at high triangularity than at low triangularity due to an improved pedestal stability [Saibene PPCF 2002, Nunes IAEA 2010, Beurskens NF2013], JET-ILW in the baseline scenario has not shown yet any major difference between the low and the high shape [Beurskens NF2014, de la Luna IAEA2014]. To date, a better confinement at high triangularity has been achieved only by N_2 seeding[Giroud NF2013]. The N_2 injection has led to a pedestal behaviour comparable to JET-C, both in terms of pedestal pressure height [Giroud PPCF2015] and ELM characteristics [Frassinetti NF2015].

The metal wall has produced confinement degradation also in ASDEX Upgrade (AUG) [Schweinzer NF2011]. Recently, the confinement degradation in the metal wall AUG was attributed to the high deuterium puff rate [Schneider PPCF2015]. The metal wall AUG tends to have higher collisionality than the carbon wall AUG, but a recent comparative study in low triangularity plasmas [Schneider PPCF2015] has shown that similar pedestal pressures can be achieved when deuterium is not puffed.

Recent results obtained in the JET-ILW baseline scenario show that H_{98}≈1 can be obtained at low triangularity when the outer strike point is moved from the horizontal target to the divertor corner, near the pump duct, where lower pedestal density and higher pedestal temperature, so lower collisionality, can be reached [Joffrin IAEA2014, de la Luna IAEA2014, Maggi NF2015]. This result, combined with the observation from the initial JET-ILW campaign, where it is shown that the baseline JET-ILW plasmas tend to have higher collisionality than the baseline JET-C plasmas [Beurskens NF2014], suggests that low collisionality operation is important in JET-ILW to achieve high performances.

The correlation between collisionality and confinement has been discussed for JET-C in [Beurskens NF2013], where, for the baseline scenario, a weak negative trend between H_{98} and collisionality has been observed. The trend is mainly ascribed to the increased pressure peaking due to increased density peaking with decreasing collisionality. The dependence of density peaking with collisionality is predicted by ITG/TEM theory (see for example [Angioni PoP 2009]) and has been experimentally observed in many devices [Angioni PRL 2003, Valovic PPCF2004, Weisen PPCF2006, Greenwald NF2006, Takenaga NF2008]. It should be pointed out that the dataset used for JET-C in reference [Beurskens NF2013] does not keep the other dimensionless parameters constant. The increase of the confinement at low collisionality has been observed also in other devices, such as DIII-D [Petty PoP1999] and NSTX [Kaye NF2013]. These two works are focused mainly on the core transport rather than the pedestal structure.

The fusion power produced by future tokamak reactors is expected to be strongly dependent on the pressure at the top of the pedestal [Shimada NF2007]. Understanding the behaviour of the pedestal structure is important for ITER, where a pedestal temperature of approximately 4keV is necessary to achieve its fusion power target [Kinsey NF2011]. The height of the pedestal pressure is determined by the interplay between the pedestal pressure gradient and the pedestal pressure width. The behaviour of the pressure gradient is, typically, reasonably described by the peeling-ballooning stability [Wilson PoP 2002, Snyder PoP2002, Huysmans PPCF 2005, Saarelma PPCF 2009, Groebner NF2013, Konz EPS2011, Urano NF2014]. However, part of the recent results show under some conditions the JET-ILW plasma in the pre-ELM phase might not have reached the peeling-ballooning stability limit yet and the modelled normalized pressure gradient tends to overestimate the experimental one [Beurskens NF2014, Saarelma PoP2015, Maggi NF2015]. Recent results on AUG-W also suggest a behaviour similar to JET-ILW [Wolfrum NF2015].

The behaviour of the pressure width is often described using the EPED1 model [Snyder, PoP 2009] which, based on kinetic ballooning modes (KBMs) constraints, predicts $w_{pe} \sim (\beta_p^{ped})^{0.5}$, where w_{pe} is the pressure pedestal width in ψ space and β_p^{ped} is the poloidal beta at the top of the pedestal. Several results from different experimental machines are consistent with the prediction from the KBM constraint [Kirk PPCF2004, Urano NF2008, Snyder PoP2009, Maggi NF2010, Beurskens PoP2011, Maggi NF2015]. However, the model does not consider the effect of the other dimensionless parameters. Concerning the pressure pedestal width dependence with ρ^*, multi-machine studies performed in AUG, DIII-D and JET-C show a very weak or no dependence with the normalized Larmor radius [Beurskens PoP2011,

Beurskens PPCF2009]. Concerning the dependence with ν*, the DIII-D results described in [Groebner NF2004] shows a reduction of the density pedestal width at high density which is ascribed to the reduction of the neutral penetration length [Onjun PoP2002]. The JET-C results described in [Leyland NF2013] show instead a positive trend between density pedestal width and density pedestal height. A similar behaviour has been recently observed in the JET-ILW hybrid scenario [Maggi NF2015]. Recent results from JT60-U also suggest a positive correlation of the pedestal width with the collisionality [Urano EPS2015, Urano NF2015].

The present work describes the role of the collisionality on the global and pedestal confinement in a dimensionless collisionality scan. Dimensionless scans are commonly used in tokamak physics to compare transport and confinement among different machines and to extrapolate the present day experiments to ITER [Luce PPCF 2008]. The energy confinement time τ_E can be expressed in terms of several dimensionless parameters (see for example [Kadomstev SJP1975, Bourdelle PPCF2008, Luce PPCF 2008]):

$$\frac{\tau_E}{\tau_B} \propto \rho^{*\alpha_\rho}\ \beta^{\alpha_\beta}\ \nu^{*\alpha_\nu}\ M^{\alpha_M}\ q^{\alpha_q}\ \varepsilon^{\alpha_\epsilon}\ \kappa^{\alpha_\kappa}\ {Z_{eff}}^{\alpha_Z}\ {M_{rot}}^{\alpha_{Mrot}} \left(\frac{T_i}{T_e}\right)^{\alpha_T} \quad (1)$$

where $\tau_B=a^2B/T\propto\rho^{*-2}B^{-1}$ is the Bohm confinement time (with a the minor radius, B the magnetic field and T the temperature), ρ* is the normalized toroidal Larmor radius, β is the plasma thermal pressure normalized to the magnetic field, ν* is the ratio of the collision frequency over the trapped electron bounce frequency, M the ratio of the ion mass over the proton mass, q the safety factor, ε the inverse aspect ratio, κ the elongation, Z_{eff} the effective charge, M_{rot} is the Mach number and T_i/T_e the ratio of the ion temperature over the electron temperature.

A set of dimensionless collisionality scans has been conducted in JET-ILW to investigate the effect of collisionality on confinement in baseline ELMy H-mode plasmas in JET-ILW. A normalised pressure scan is planned for the upcoming experimental JET campaign. In the present work, the pedestal collisionality is changed by a factor ≈10, while the other parameters in equation (1) are kept as constant as possible. This is further discussed in Section 2.

This work describes the dependence of the global confinement, of the pedestal confinement and of the pedestal structure (with particular emphasis on the pressure gradient and the pressure width) on collisionality. The experimental results are then discussed in term of comparison with the peeling-ballooning stability and with the EPED1 model predictions. The paper is organized as follows. Section 2 describes the dataset used, discussing the dimensionless parameters and the corresponding operational parameters used. Section 3

describes the dependence of the global and pedestal confinement on collisionality. Section 4 describes the pedestal structure. Section 5 compares the experimental results with the EPED1 model. Section 6 discusses the peeling-ballooning stability. Section 7 describes the effect of collisionality on the scrape-off layer density. The conclusions are presented in Section 8.

2. DESCRIPTION OF THE DATABASE

2.1 Plasma Scenario

The work has been carried out on a set of JET-ILW plasmas with β_N in the range ≈1.5-1.8. To date, differences in the confinement between high and low triangularity in the JET-ILW baseline scenario have been observed only with N_2 seeding [Giroud NF2013, Giroud PPCF2015]. The present plasmas have been performed without N_2, so the low triangularity shape has been chosen for simplicity. The divertor configuration has the outer strike point on the divertor corner near the pump duct. This configuration allows operations at low Greenwald density (f_{GW} down to 0.55-0.6) and allows the density control via gas puffing. The plasmas are heated mainly via NBI with a real time control to achieve the desired β value. The NBI power is in the range 11-22MW. The ICRH power is in the range 1-4MW and is used to reduce W accumulation in the core.

The present plasmas are in a Type I ELMy H-mode as suggested by the increase of the ELM frequency with the power through the separatrix. Moreover, the pedestal temperature T_e^{ped} is higher than 400-500eV, while in JET-ILW the Type III ELMs occurs at T_e^{ped} lower than 300eV [Beurskens NF2014, Giroud PPCF2015]. Finally, the ELM energy losses are large compared to the Type III ELMs, with a value (W_{ELM}/W_{ped}>8-10%) relatively consistent with Type-I ELM losses [Loarte PPCF2003, Frassinetti NF2015]. The details of the ELM behaviour with collisionality will be discussed elsewhere.

2.2 Plasma Parameters

The collisionality scan is achieved by changing the gas fuelling level. The normalized pressure and the normalized Larmor radius are kept constant by varying the NBI power and the plasma current. The magnetic field is changed in order to keep q_{95}≈3. Four collisionality scans have been achieved at four different β_N values. The volume averaged collisionality $\langle \nu^* \rangle$, the volume averaged normalized poloidal Larmor radius $\langle \rho_p{}^* \rangle$ and the normalized thermal

beta β_N are shown in figures 1(a) and 1(b). The collisionality and the Larmor radius have been calculated as:

$$\nu^*=6.92\cdot10^{-18} n_e R q_{95} Z_{eff} \ln\Lambda/(\varepsilon^{3/2} T_e^{\,2}) \quad (2)$$

$$\rho_p^*=4.57\cdot10^{-3} (2T_i)^{1/2}/(aB_p) \quad (3)$$

where $B_p=\mu_0 I_p/c$ is poloidal magnetic field with c the length of the last closed flux surfaces.

In the calculation of ρ^*, it has been assumed $T_e=T_i$ which, for this dataset, is a valid assumption, as later discussed. The volume averaged collisionality has been varied by a factor 5 from $\langle\nu^*\rangle\approx$0.03-0.04 to $\langle\nu^*\rangle\approx$0.15 for all the four β_N levels. The Larmor radius is kept constant as much as possible in the range $\langle\rho_p{}^*\rangle \approx$ 2.5%-2.9%. Since q_{95} is constant, also $\langle\rho_t{}^*\rangle$ remains constant. The dataset shown in figure 1(a) and 1(b) has been used to investigate the dependence of the global confinement and the pedestal confinement on collisionality (Section 3).

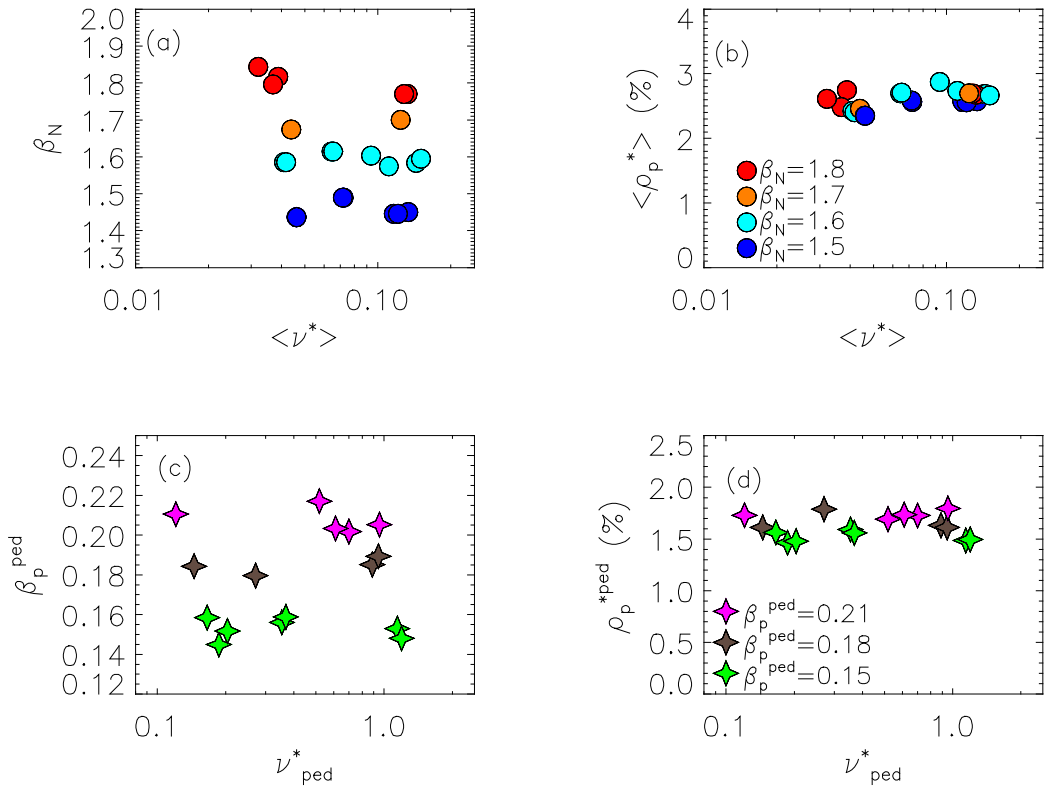

Figure 1. *Range of the dimensionless parameters. Frames (a) and (b) show the range of variation of the volume averaged collisionality, normalized beta and volume average Larmor radius. The colours highlight four different collisionality scans achieved at different β_N values. This dataset is used to study the global confinement. Frames (c) and (d) show the range of variation of the pedestal collisionality, poloidal pedestal beta and pedestal Larmor radius. The colours highlight three different collisionality scans achieved at different β_p^{ped} values. This dataset is used to study the pedestal structure.*

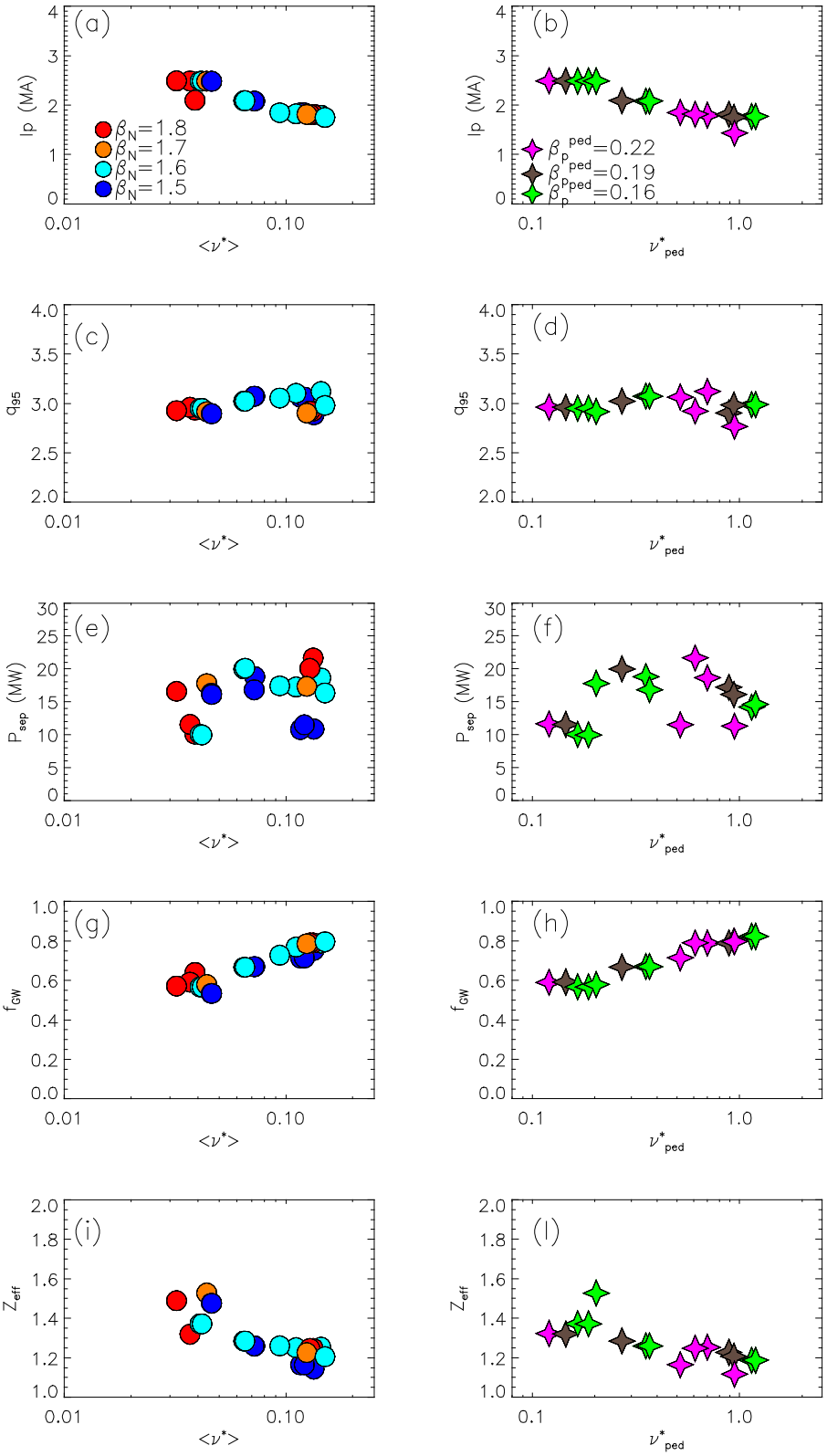

Figure 2. *Variation with collisionality of the main operational parameters for the dataset used to study the global confinement (left column) and for the dataset used to study the pedestal structure (right column). Frames (a) and (b) show the plasma current, frames (c) and (d) show q_{95}, frames (e) and (f) the power through the separatrix, frames (g) and (h) the Greenwald density fraction and frames (i) and (l) show the effective charge.*

However, the change in collisionality affects the density peaking and therefore also the ratio between core and pedestal pressure. This implies that, in a collisionality scan, a dataset with constant β_N has slightly different pedestal beta. For this reason, a second dataset is considered when investigating the pedestal structure (Section 4). Figures 1(c) and 1(d) show the dataset with constant β_p^{ped}. Three collisionality scans at three different β_p^{ped} values have been done. The pedestal poloidal beta is calculated as:

$$\beta_p^{ped}=p^{ped} / [B_p^2/(2\mu_0)] \quad (4)$$

where p^{ped} is the pedestal thermal pressure calculated assuming $T_i=T_e$ and $n_i=n_e(5-Z_{eff})/4$ (assuming the Be as main impurity). The pedestal collisionality and the pedestal Larmor radius are calculated using equations (2) and (3) with the density and temperature calculated at the pedestal top. The corresponding pedestal collisionality ν^*_{ped} varies by a factor 10, while the pedestal normalized Larmor radius is constant at $\rho^*_{ped}\approx$1.6-1.8%.

The main operational parameters used in the two datasets are shown in figure 2. The plasma current is shown in figures 2(a) and 2(b). The plasma current is increased from Ip≈1.7MA at high ν^* to Ip≈2.5MA at low ν^*. The safety factor is shown in figure 2(c) and 2(d) and is kept approximately constant in the range q_{95}=2.9-3.1 by changing the field from B_T=1.8T at high ν^* to B_T=2.4 at low ν^*. The power through the separatrix P_{sep} is in the range 10-22MW, figures 2(e) and 2(f). P_{sep} has been calculated as $P_{sep}=P_{NBI}+P_{\Omega}+P_{ICRH}-P_{rad,bulk}-dW/dt$. The Greenwald density fraction is shown in figures 2(g) and 2(h) and is controlled via gas puff. The gas flow injected from the valve used for density control is in the range $\Gamma_{D2}\approx10^{22}$(e/s) to $\Gamma_{D2}\approx5\cdot10^{22}$(e/s). The effective charge is measured with a line integrated filter spectrometer and is shown in figures 2(i) and 2(l). It was not possible to keep Z_{eff} constant throughout the entire scan, but the variation is relatively small, from $Z_{eff}\approx$1.2 at high ν^* to $Z_{eff}\approx$1.5 at low ν^*, figure 2(i). For the dataset used to study the pedestal structure, the range of variation of Z_{eff} is even smaller, from $Z_{eff}\approx$1.2 at high ν^* to $Z_{eff}\approx$1.4 at low ν^*, figure 2(l).

The ion temperature is similar to the electron temperature both in the core and at the pedestal with $T_i/T_e\approx$1.0-1.05 and with no systematic variation versus ν^* (within the experimental uncertainty). This has been verified for two shots at low collisionality ($\langle\nu^*\rangle\approx$0.03-0.04) and two shots at high collisionality ($\langle\nu^*\rangle\approx$0.13-0.14). The charge exchange measurements are not available for the entire datasets.

The Mach number has been calculate as $M_{rot}=v_\phi/v_{th}$, where v_ϕ is the toroidal velocity and $v_{th}=\sqrt{eT_i/m}$ is the thermal velocity. It was not possible to keep perfectly constant the Mach number which tends to be larger at low collisionality ($M_{rot} \approx 0.45$ *at* $\rho_{tor}=0.5$) than at high collisionality ($M_{rot} \approx 0.3$ *at* $\rho_{tor}=0.5$). A scaling analysis in JET-C [De Vries NF2008] shows that the energy confinement scales as $\tau_E \propto (M_{rot})^{-0.21}$. Assuming a similar scaling in JET-ILW, the present difference in the Mach number would affect the energy confinement by ≈9% (much less than what experimentally observed, from τ_E≈0.1s at high collisionality to τ_E≈0.25s-0.3s at low collisionality). So, for the present dataset, it is reasonable to assume that the effect of M_{rot} is negligible compared to the effect of the collisionality.

As a final remark, due to the fact that JET-C tend to have lower ν*, higher β and significantly higher Z_{eff} than JET-ILW, it has been not possible to identify a set of JET-C plasma with dimensionless parameters similar to the present JET-ILW dataset. So a comparison between JET-C and JET-ILW cannot be discussed in the present paper.

2.3 Diagnostics for the pedestal structure

The High Resolution Thomson Scattering (HRTS) [Pasqualotto RSI2004] is used to measure electron temperature and density. Only the profiles in a stationary phase are considered for the analysis of the pedestal structure. The stationary phases used are longer than 0.5s and at least four energy confinement time long (τ_E≈0.1s-0.25s). The pre-ELM density and temperature profiles of each stationary phase are then fitted with a modified hyperbolic tangent function [Groebner NF2001] to estimate the pedestal height and pedestal width:

$$mtanh(r)=\frac{h}{2}\left(\frac{(1+sx)e^{x}-e^{-x}}{e^{x}+e^{-x}}+1\right) \qquad \text{with} \quad x=\frac{p_{pos}-r}{2w_r} \tag{5}$$

where r is the radius in real space along the HRTS line of sight, h is the pedestal height, p_{pos} is the pedestal position and w_r the pedestal width in real space. The parameter s allows the presence of a linear slope in the inner side of the pedestal. In the scrape-off layer (SOL) outside the pedestal, it is assumed that both density and temperature are negligible. This assumption works very well for the temperature and it is reasonable at medium and low collisionality for the density. At very high collisionality, the SOL density starts to be not negligible. This is further investigated in Section 7, where the effect of a fitting function that allows $n_e^{SOL}\neq 0$ is discussed, showing that the impact on the pedestal width and gradient is minimal.

To estimate the pedestal width for the density and the temperature, only the profiles in the pre-ELM phase are considered. The fits are repeated considering the profiles in several pre-ELM phases in order to verify the stability of the result. In the fitting procedure, the effect of the HRTS instrument function is taken into account. The details of the HRTS fitting method are described in reference [Frassinetti RSI2014].

The electron pressure pedestal height is determined from the temperature and density pedestal height, $p_e^{ped}=k_B \cdot T_e^{ped} \cdot n_e^{ped}$. The pressure pedestal width is estimated using the definition implemented in EPED1, as the average between density and temperature pedestal widths, $w_{pe}=(w_{ne} + w_{Te})/2$.

The reflectometer data [Sirenelli RSI2010] are used to cross check the density width estimations obtained with the HRTS. The reflectometer is available only for a limited set of data at low and medium collisionality but in general the two diagnostics produces similar results within the experimental uncertainty. The Li-beam diagnostic is used to cross-check the HRTS data in SOL. Further discussions are presented in Section 7.

3. GLOBAL and PEDESTAL CONFINEMENT

3.1 Confinement factor and global confinement scaling

The initial results from the first JET-ILW campaigns have shown a reduction of the confinement in the baseline scenario with a confinement factor in the range H_{98}=0.8-0.9 [Beurskens 2014]. Good confinement with H_{98}≈1.0 has been recently recovered by moving the outer strike point on the divertor corner allowing operation at a lower density [de la Luna IAEA 2014, Joffrin IAEA 2014, Maggi NF2015].

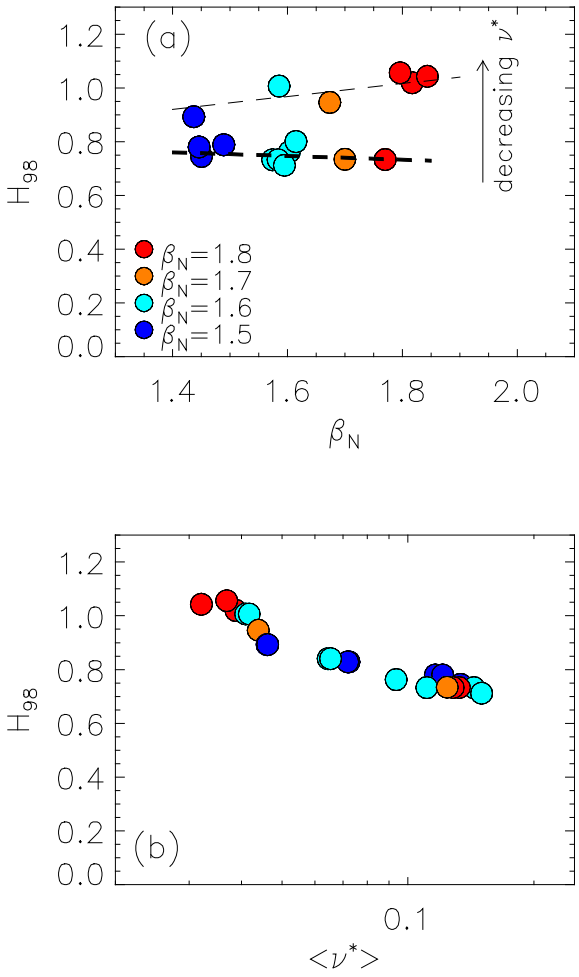

Figure 3. *Correlation of H_{98} with β_N (a) and with volume averaged ν* (b). The dashed lines in frame (a) shows a linear fit to the data with low collisionality,* ν*<0.05 (thin dashed) and high collisionality, ν*>0.1 (thick dashed).

Figure 3(a) shows the correlation between H_{98} and β_N for the present dataset. The thin dashed line shows a linear fit to the low collisionality shots (<ν*> <0.05) and the thick dashed line to the high collisionality (<ν*> >0.1).

The JET-ILW plasmas at high ν* show no dependence of H_{98} with β_N and the confinement factor remains at H_{98}≈0.8. The usual positive trend between H_{98} and β_N [Beurskens NF2013] is re-established at low ν*. H_{98}≈1.0 is reached at low collisionality and high β_N.

JET-C data cannot be easily compared to the present dataset because the dimensionless parameters are not matched, however, it is worth noticing that the present low ν* plasmas (<ν*> <0.05) reach β_N and H_{98} comparable to the low-δ baseline JET-C plasmas discussed in [Beurskens NF2013].

The trend between H_{98} and ν* is shown in figure 3(b). A clear increase of the confinement factor with decreasing ν* can be observed.

The present ν* scan has been performed keeping the other dimensionless parameters as constant as possible (apart from a 15-20% variation in Z_{eff}). So equation 1 can be expressed in a simplified form:

$$B\tau_E \propto \nu^{*\alpha_\nu} \quad (6)$$

allowing the estimation of the parameter α_ν. Figure 4 shows the correlation between $B\tau_E$ and the local ν* calculate at ρ_{tor}=0.6. The local ν* has been chosen instead of the volume averaged ν* for a consistent comparison with earlier results [Luce PPCF2008]. The energy confinement time is calculated from the total thermal stored energy, as later discussed in equation (7). The correlation between the normalized energy confinement time and ν* is clear for all the four levels of β_N. Note that the dimensionless parameter related to the pressure in equation 1 is the toroidal β, not the Troyon limit related to the normalized β ($\beta_N=\beta aB_T/I_p$). However, since the scans have been performed at constant q_{95}, keeping β_N constant automatically implies that the toroidal β is constant.

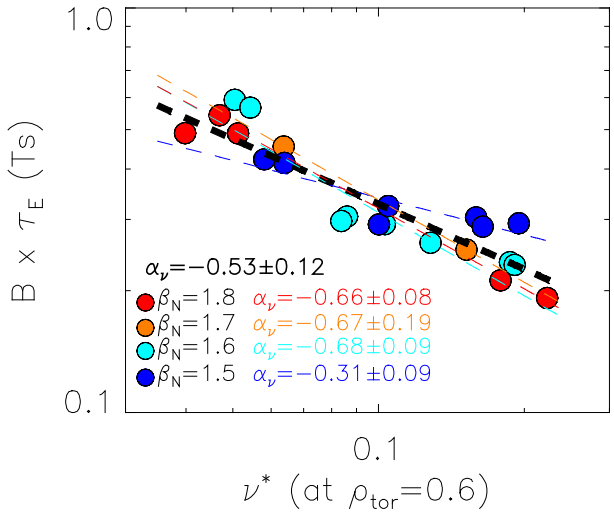

Figure 4. *Correlation between the normalized confinement time and the local collisionality calculated at at ρ_{tor}=0.6 where ρ_{tor} is the square root of the toroidal flux normalized at the LCFS. The coloured dashed lines show the fits of the four different beta values separately. The thick line shows the fit of the entire dataset.*

By fitting the data of figure 4 using the expression of equation 6, the parameter α_ν is estimated approximately $\alpha_\nu \approx -0.67$ for the scans obtained at β_N=1.6, 1.7 and 1.8. The collisionality scan at low beta (β_N=1.5) produces a significant lower value, with $\alpha_\nu \approx -0.31$.

The difference in α_ν between the scan at β_N=1.5 and at the scans higher β_N is not fully understood. However, as discussed in the remaining part of this section, we might speculate that α_ν is related to β_N.

The present estimation of the parameter α_ν for the lowest β_N dataset is in good agreement with the JET-C result discussed in [Cordey EPS2004, McDonald IAEA2004, Luce PPCF2008], which are in the range $\alpha_\nu \approx -0.3$ to $\alpha_\nu \approx -0.4$. The JET-C results have been obtained at $1.25<\beta_N<1.4$, so in a β_N range close to the present low β_N case.

The present α_ν estimation using the three high beta cases are similar to those obtained in NSTX [Kaye NF2013], DIII-D and C-mod [Petty PoP1999, Luce PPCF2008]. In particular,

the DIII-D results have been obtained at β_N=1.65-1.7, so in a range comparable to the present high beta scans.

The origin of the different α_ν at low and high β_N might be related to the pedestal behaviour. As discussed in Section 3.4, in particular in figure 8, the pedestal pressure at low β_N does not increase significantly with ν^* and the confinement improvement with decreasing ν^* is mainly driven by the core. Instead, at high β_N, the reduction of ν^* is related to a significant increase in the pedestal pressure and in the core pressure. α_ν is a global parameter that describes the global confinement and cannot discriminate the different behaviour of core and pedestal. So, a possible explanation for the difference in α_ν is that, at low beta, α_ν reflects only the improvement in the core stored energy, while, at high beta, α_ν reflects the improvement in both the core and the pedestal stored energies.

3.2 Total, core and pedestal thermal stored energy

The improvement of confinement at low ν^* is related with the increase of the thermal stored energy. The thermal energy W_{th} is calculated by volume integrating the pressure profiles:

$$W_{th} = \frac{3}{2} k_B \int \left(T_e n_e + T_i n_i \right) dV \tag{7}$$

assuming T_i=T_e and calculating n_i using Z_{eff} as described in Section 2.2. The pedestal energy and core energy are calculated as

$$W_{th}^{ped} = \frac{3}{2} k_B \left[n_e^{ped} T_e^{ped} + n_i^{ped} T_i^{ped} \right] \cdot \left[V_{ped} + \frac{1}{2} (V_{tot} - V_{ped}) \right] \tag{8}$$

$$W_{th}^{core} = W_{th} - W_{th}^{ped} \tag{9}$$

The correlation of the stored energy with the volume averaged ν^* is shown in figure 5. The total stored energy increases from W_{th}≈2.4-2.5MJ at high ν^* to W_{th}≈4.0-4.5MJ at low ν^*, figure 5(a). This is due to an increase both in the core energy and in the pedestal energy, figures 5(b) and 5(c) respectively. However, the increase in the W_{th} is stronger in the core than in the pedestal as can be seen with a non-linear regression: $W_{th} \propto \langle\nu^*\rangle^{-0.39}$, $W_{th}^{core} \propto \langle\nu^*\rangle^{-0.41}$ and $W_{th}^{ped} \propto \langle\nu^*\rangle^{-0.26}$. In fact, the core energy increases by a factor two, from W_{th}^{core}≈1.6-1.8MJ to W_{th}^{core}≈3.4-3.8MJ, while the increase in the pedestal energy is slightly smaller, from W_{th}^{core}≈0.7MJ to W_{th}^{core}≈1.1-1.2MJ. The regression has been performed also for each single β_N level and no significant variation is observed within the error bars. The only difference occurs in the W_{th}^{ped} scaling at the lowest β_N level which has an exponent -0.11±0.09.

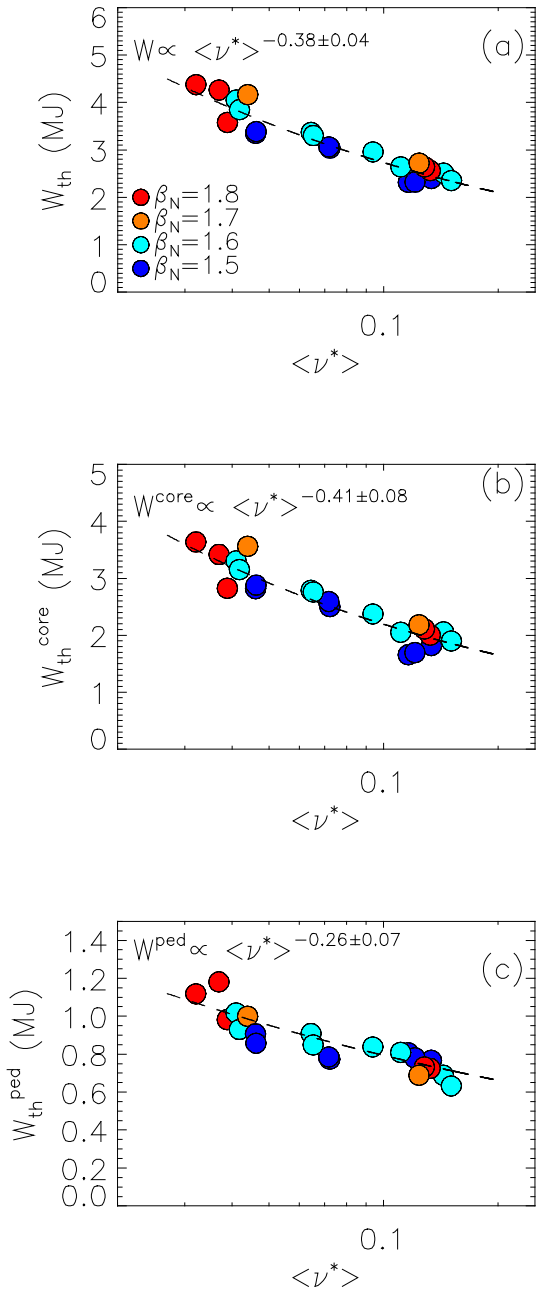

Figure 5. *Correlation between the thermal energy and the collisionality. (a) total thermal energy, (b) core energy and (c) pedestal energy.*

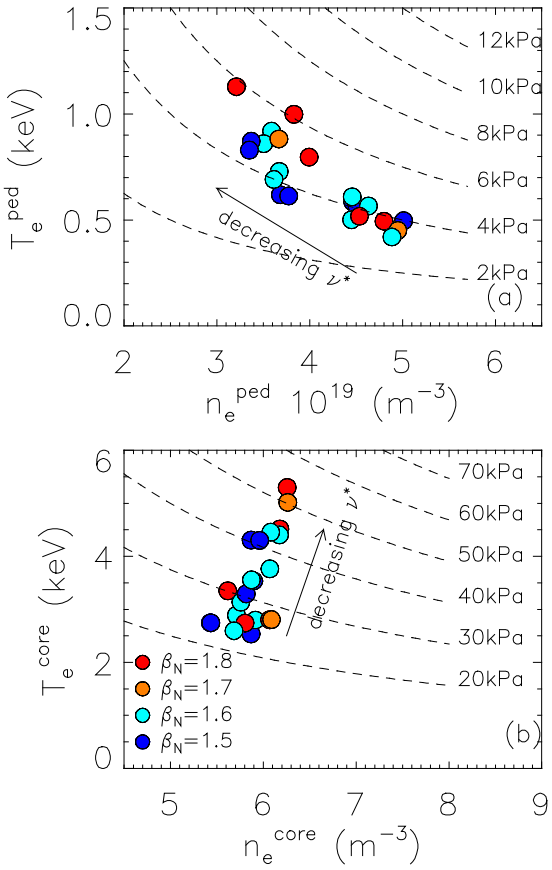

Figure 6. *Pedestal temperature versus pedestal density (a) and core temperature versus core density (b). The core values are calculated at ρ_{tor}=0.3, where ρ_{tor} is the square root of the normalized toroidal flux. The dashed lines show the isobar curves.*

To understand in more details the behaviour of the core and the pedestal stored energy, figure 6(a) shows the pedestal temperature T_e^{ped} versus the pedestal density n_e^{ped} and figure 6(b) the core temperature T_e^{core} versus the core density n_e^{core}. The reduction of ν* is related to the reduction of n_e^{ped} and to the increase of T_e^{ped}. The increase of T_e^{ped} is stronger than the reduction of n_e^{ped} and, consequently, the low ν* plasmas have higher electron pedestal pressure p_e^{ped}. The pedestal pressure increases from p_e^{ped}≈3.5kPa to p_e^{ped}≈6kPa. In the core, a significantly different behaviour is observed. The core density has a weak increase with decreasing collisionality, while the core temperature shows a strong increase. The core

pressure increases from p_e^{ped}≈20kPa at high ν* to p_e^{ped}≈50kPa at low ν*. Basically, the increase of the core pressure tends to be stronger than the increase of the pedestal pressure.

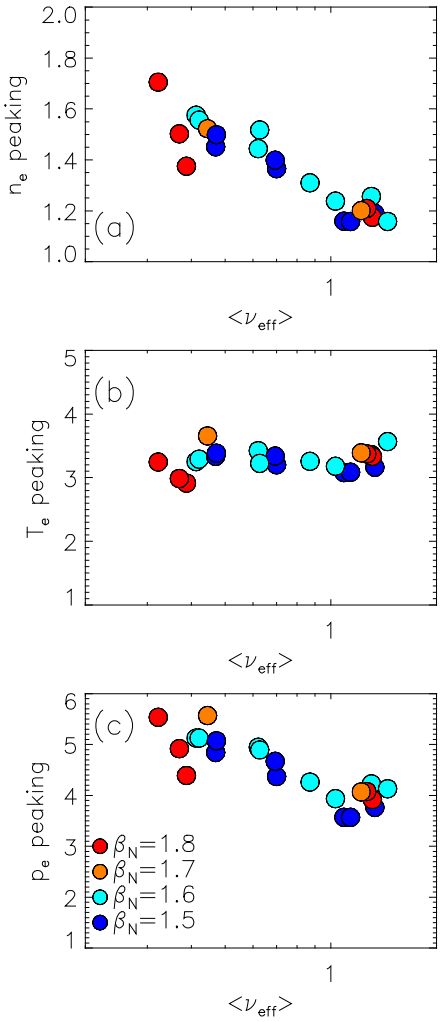

Figure 7. *Density peaking (a) temperature peaking (b) and pressure peaking (c) versus the effective collisionality. The peaking is calculated as profile at ρ_{tor}=0.3 divided by the profiles at ρ_{tor}=0.8 to be consistent with [Beurskens NF2014].*

The stronger increase in the core confinement than in the pedestal confinement is due to the T_e profiles stiffness and to the n_e profile peaking at low collisionality, as described in the next Section.

3.3 Profile peaking

The difference in the core and pedestal temperature and density is related to the behaviour of the corresponding profiles. Figure 7(a) shows the density peaking versus the volume averaged effective collisionality <ν_{eff}> and figure 7(b) the temperature peaking. Here, <ν_{eff}> is used instead of <ν^*> to have a more direct comparison with earlier results (see for example [Maslov NF2009, Beurskens NF2014]).

The density peaking scales very clearly with the collisionality, as already observed in several devices [Angioni PRL 2003, Valovic PPCF2004, Weisen PPCF2006, Greenwald NF2006, Takenaga NF2008, Maslov NF2008, Beurskens NF2014]. The temperature profiles are instead stiff and no clear dependence with collisionality is observed. This is consistent with earlier analysis in JET-ILW, as discussed in [Beurskens NF2014].

In summary, the increase of the core thermal energy is due to two factors: (i) the increase in T_e^{core} which is driven by the increase in T_e^{ped} via the T_e profile stiffness and (ii) the increase of the pressure peaking [figure 7(c)] due to the increase of the density peaking. The increase in the pedestal pressure is instead related only to the increase of T_e^{ped} (while the pedestal density decreases with increasing collisionality).

The physical reason for the increase of the pedestal pressure is discussed in Sections 5 and 6.

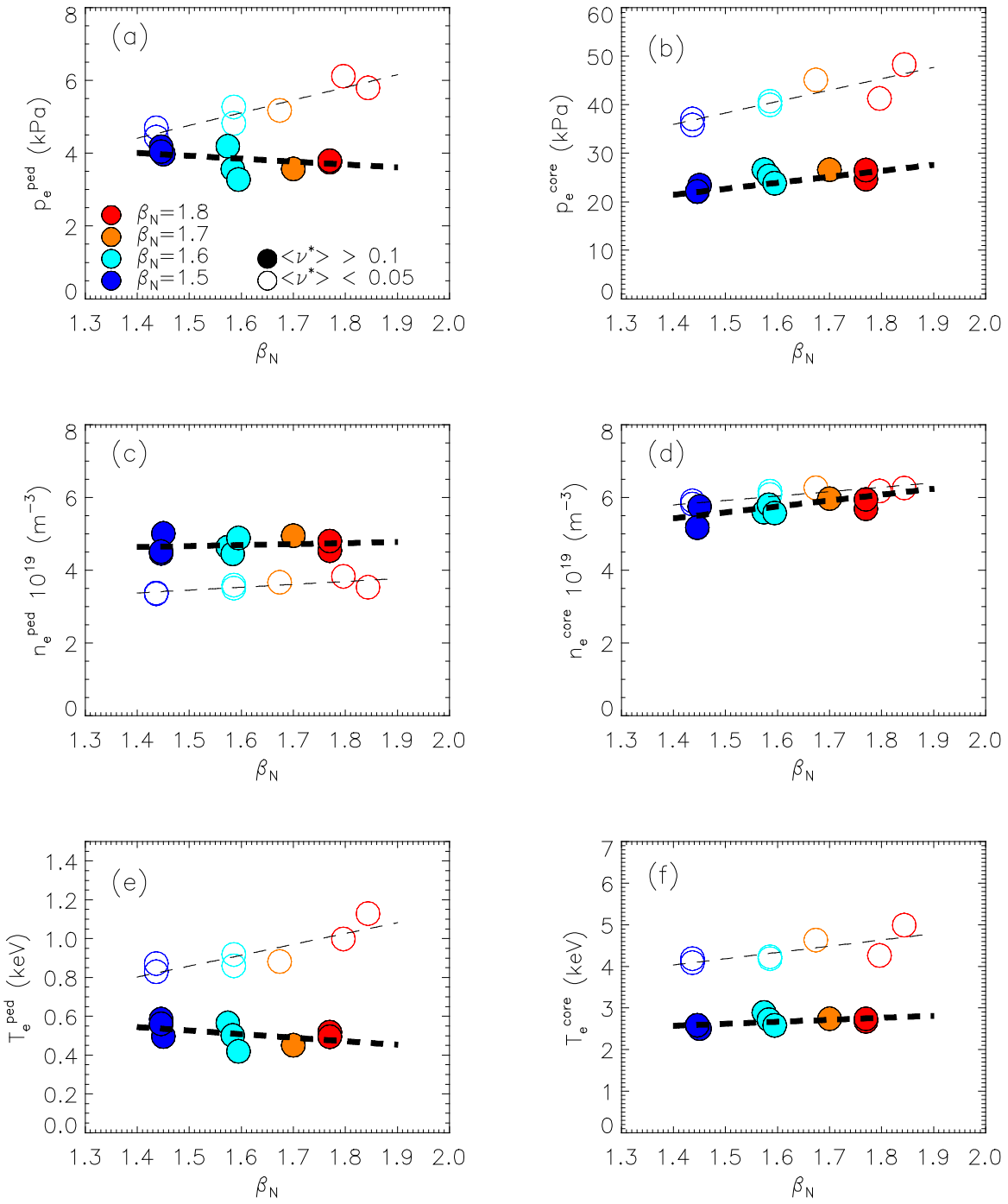

Figure 8. *Electron pressure (first row), density (second row) and temperature (third row) at the pedestal (left column) and in the core at ρ_{tor}=0.3 (right column) versus β_N. Only the lowest collisionality plasmas (<ν^*> <0.05), empty symbols, and the highest collisionality plasmas (<ν^*> >0.1), full symbols, are shown. The thin and thick dashed lines shows a linear fit to the low ν^* plasmas and to the high ν^* plasmas respectively.*

3.4 Difference between high and low collisionality.

The difference in the behaviour of high and low collisionality plasmas is clear in figure 3(a). At high collisionality, the increase in β_N is not related to any increase in H_{98}. At low collisionality, a positive trend between β_N and H_{98} is present. This is mainly due to a pedestal

effect, as discussed in figure 8 where the pressure, density and temperature at the pedestal and in the core are shown versus β_N. The range in β_N is very limited, but the trends in figure 8 are sufficiently clear to obtain a preliminary explanation for the difference in the trends of H_{98} vs β_N at low and high collisionality.

To emphasize the difference, figure 8 shows only the plasmas with the highest collisionality ($<\nu^*> > 0.1$, full symbols) and with the lowest collisionality ($<\nu^*> < 0.05$, empty symbols). At low collisionality, both the pedestal and the core pressure increases with β_N. At high collisionality, only the core pressure increases while the pedestal pressure is approximately constant (or has a weak negative trend) with β_N [figures 8(a) and 8(b)]. This is not due to the density behaviour as both the pedestal density and the core density have similar trends with β_N, figures 8(c) and 8(d). The difference is due to the pedestal temperature, figure 8(e). The pedestal temperature increases with β_N at low collisionality, while no trend or even a weak reduction with β_N is present at high collisionality. The pedestal temperature behaviour affects also the core via the T_e profile stiffness. In fact, the increase of T_e^{core} with β_N is less strong at high than at low collisionality, figure 8(f).

The origin of the degraded pedestal temperature at high collisionality is discussed in Section 6.

Due to the limited range in β_N of the present dataset, no strong claims on the beta scaling are possible. An extension of the beta range is planned for the next experimental JET campaign.

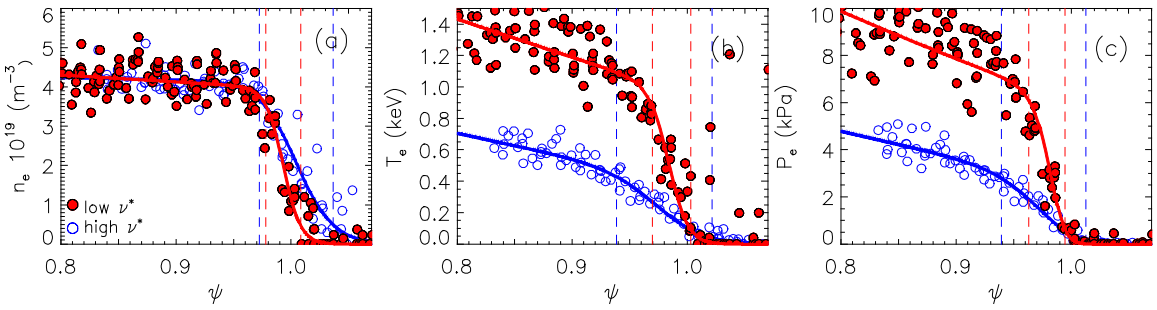

Figure 9. *Pre-ELM profiles of electron density (a), temperature (b) and pressure (c) in the pedestal region for two plasmas with β_p^{ped}≈0.21 and ρ_p^{*ped}≈1.7% at low collisionality (ν^*_{ped}≈0.1, red full dots) and high collisionality (ν^*_{ped}≈0.9, blue empty dots). The vertical dashed lines highlight the pedestal width.*

4. THE PEDESTAL STRUCTURE

The pedestal structure for a high and a low collisionality shot at high beta is shown in figure 9. Note that, hereafter, the dataset with the dimensionless parameters matched at the pedestal top is used (second row in figure 1). Figure 9(a) shows the pedestal density, figure 9(b) the pedestal temperature and figure 9(c) the pedestal pressure. The reduction of collisionality is associated with an increase in the pedestal temperature while no difference is present in the pedestal density. The overall effect is an increased pedestal pressure. Note the difference between the pedestal density behavior in figure 9(a), where no trend is observed with ν^*_{ped} and figure 6(a), where the reduction of the pedestal density with decreasing $<\nu^*>$ is observed. This is due to two reasons: (I) in a dimensionless collisionality scan the density is supposed to remain constant and (II) the change in the collisionality affect the density peaking. When the scan is performed in ν^*_{ped}, the pedestal density remains constant, while when the scan is performed in $<\nu^*>$, the volume averaged density remains constant. So, due to the difference in the density peaking, a constant volume averaged density implies that an increase in the core density must be compensated by a decrease in the pedestal density.

Another important effect that can be observed in figure 9 is the reduction of the pedestal width with decreasing collisionality, both in the density, in the temperature and, consequently, in the pressure. A consistent behaviour has been observed in JET-C in baseline plasmas [Leyland NF2013] and in JET-ILW in hybrid plasmas [Maggi NF2015], where the increase of the pressure width at high gas was shown.

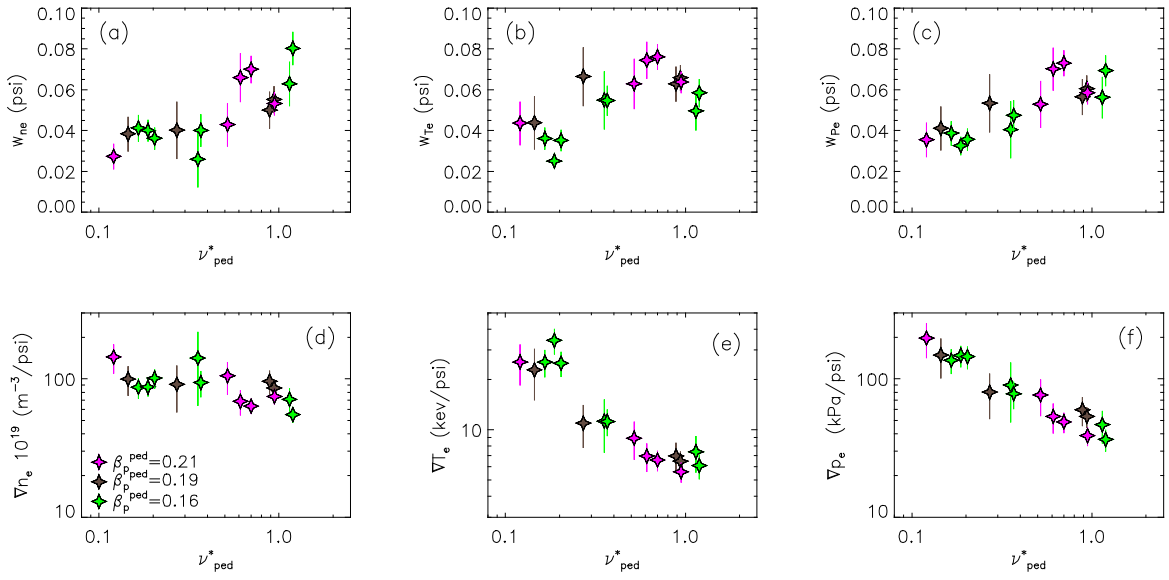

Figure 10. *Frames (a), (c) and (c) show the correlation of the pedestal width with the pedestal collisionality. Frames (d), (e) and (f) show the correlation of the pedestal gradient with the pedestal collisionality.*

The behaviour of the pedestal width for the entire dataset is shown in figure 10(a) for the density, figure 10(b) for the temperature and figure 10(c) for the pressure. A positive trend between the pedestal width and the collisionality is present. The behaviour of the pressure width is the most relevant for the pedestal height predictions, so a non-linear regression for the pressure width has been attempted using the following power law:

$$w_{pe} = c\left(\nu^*_{ped}\right)^{\gamma_\nu}\left(\beta_p^{ped}\right)^{\gamma_\beta} \tag{10}$$

	γ_ν	γ_β	c
OLS	0.26±0.04	0.59±0.27	0.19±0.11
GLS	0.27±0.05	0.71±0.34	0.25±0.16

Table 1. *Parameters of the non-linear regression of the pedestal pressure width with collisionality and beta.*

The β_p^{ped} term has been included because the fit has been performed considering the entire dataset, without performing the fit separately for each "constant beta" scan. The regression has been done using ordinary least squares (OLS) and geodesic least squares (GLS) [Verdoolaege, Entropy 2015] using a bootstrapping method which employs a resampling technique that generates a large number of synthetic datasets from the original data, by resampling with replacement. Then, both OLS and GLS were carried out on each of these data sets and the average of all the obtained coefficients was calculated. The results are reported in table 1. As far as the dependence on collisionality is concerned, the two methods produce comparable results, with an exponent $\gamma_\nu \approx 0.26$. Interestingly, despite the very narrow range of variation of beta, the width scaling with β_p^{ped} is consistent, within the uncertainty, with the KBM constraint implemented in EPED1, which assumes $\gamma_\beta=0.5$: $w_{\mathrm{pe}} = 0.076\sqrt{\beta_p^{ped}}$, as described in [Snyder PoP2009].

The level of consistency between the present dataset and the KBM constraint is clear in figure 11(a), where the pressure width versus β_p^{ped} is shown. At low collisionality, the experimental width is in reasonable agreement with the KBM constraint, while at high collisionality a major discrepancy is observed.

In figure 11(b), the correlation of the pressure width normalized to $(\beta_p^{ped})^{0.5}$ versus the collisionality is shown. Once the dependence with β_p^{ped} is removed, the correlation of the pressure width with the collisionality is slightly more clear than in figure 10(c). The deviation from the KBM constraint prediction at high ν* suggests that the present models are not sufficient to describe in detail the pedestal width behaviour. Nonetheless, the predictions are very reasonable at low collisionality. The vertical dashed line shows the pedestal collisionality expected for ITER. This has been calculated with equation (2) using the value in reference [Loarte PPCF2003] and assuming Z_{eff}=1.3 for ITER. Since no dependence of the pedestal width with ρ* has been observed so far [Beurskens PPCF2009, Beurskens PoP2011], the extrapolation to ITER might be reasonable even if the normalized Larmor radius is not considered. The present result suggests that the KBM constraint might be a valid assumption for the estimation of ITER pedestal width.

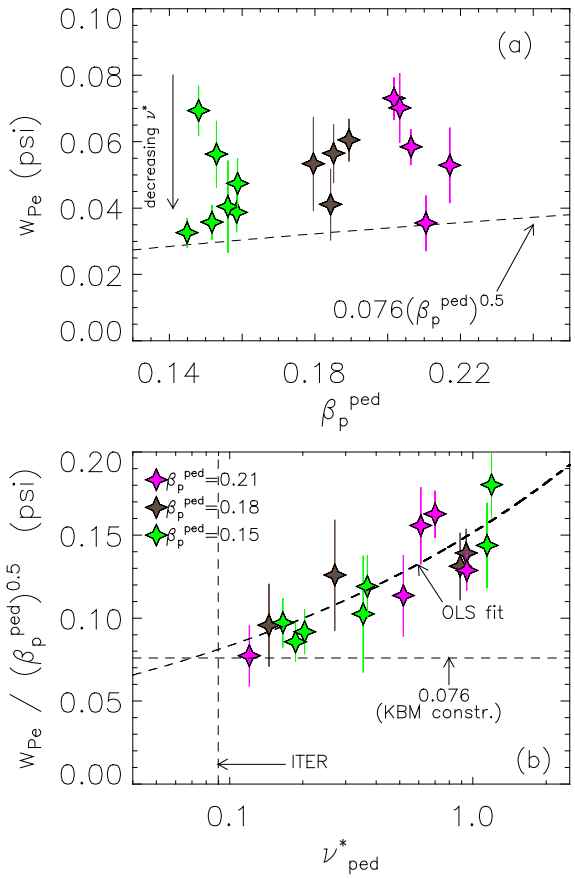

Figure 11. *(a) Correlation of the pressure pedestal width with β_p^{ped}. The dashed line shows the EPED1 predictions. (b) Correlation of pressure width with the β_p^{ped} dependence removed versus the pedestal collisionality.*

To complete the discussion on the pedestal structure, the pedestal gradients for the entire dataset are shown in figure 10(d) for the density, 10(e) for the temperature and 10(f) for the pressure. It is interesting to note that the dependence of the gradient with collisionality is weaker for the density than for the temperature. This is because the increase of ∇n_e^{ped} with decreasing collisionality is due mainly to the narrowing of the width, while increase of ∇T_e^{ped} with decreasing collisionality is due to both the narrowing the width and the increase of the T_e^{ped}.

5. COMPARISON OF THE PEDESTAL PRESSURE WITH EPED1.

To start investigating the origin of the pedestal improvement at low collisionality, the comparison of the experimental data with the EPED1 predictions has been performed for three shots at high beta ($\beta_p^{ped} \approx 0.21$) and with low, medium, high collisionality.

The comparison between the experimental pressure and the EPED1 predicted pressure is shown in figure 12. The inputs to EPED1 are the experimental pedestal density, the total beta, the plasma shape, the plasma current and the toroidal magnetic field. The pedestal height is calculated from the intersection of peeling-ballooning constraint (calculated with the ELITE code [Wilson PoP2002] using $\gamma > \omega^*_{max}/4$ as the stability criterion, where ω^*_{max} is the maximum of the ion diamagnetic frequency in the pedestal region) and the KBM constraint as described in [Snyder PoP2009]. Figure 12(a) shows the correlation of experimental p_e^{ped} with the pedestal collisionality for the entire dataset and the corresponding p_e^{ped} predictions. A good qualitative agreement is observed but EPED1 tends to overestimate the pedestal pressure. The overestimation increases with collisionality: at low ν^*_{ped} the difference is ≈15%, at medium and high ν^*_{ped} the EPED1 predictions are respectively ≈30% and ≈35% higher than the experimental results. The origin of this behaviour is discussed in the next section along with the stability analysis results.

To complete the comparison with EPED1, the correlation between the pressure width and the pedestal collisionality is shown in figure 12(b). As already described, the KBM constraint reproduces the experimental width only at low collisionality.

The EPED1 results in figure 12(a) might suggest that EPED1 predicts an improvement of the pedestal stability with decreasing collisionality, but this is not case. This has been investigated by determining the normalized pressure gradient at the stability limit, α_{max}, which, according to the definition in [Miller PoP1998] is:

$$\alpha = -\frac{2\partial_\psi V}{(2\pi)^2}\left(\frac{V}{2\pi^2 R_0}\right)^{1/2}\mu_0 p' \qquad (11)$$

with V the plasma volume, R the major radius and p' the pressure derivative in the poloidal flux ψ. In this collisionality scan, EPED1 does not observe any significant change of α_{max} which is in the range ≈4.2-4.4 both at low and high ν^* [this is discussed also later in figure 15(a)]. So, EPED1 does not predict any improvement in the pedestal stability at low collisionality.

This result is not surprising. The main parameters that affect the pedestal stability are the normalized pressure, the plasma shape, the pedestal width and the pedestal position of density and temperature. The three plasmas analysed with EPED1 have the same shape and similar

normalized pressure. Moreover, EPED1 assumes no change in the pedestal widths because β_p^{ped} is constant. Finally, EPED1 assumes no difference in the pedestal position of density and temperature. So, for this dataset, no difference in the pedestal stability can be expected from EPED1.

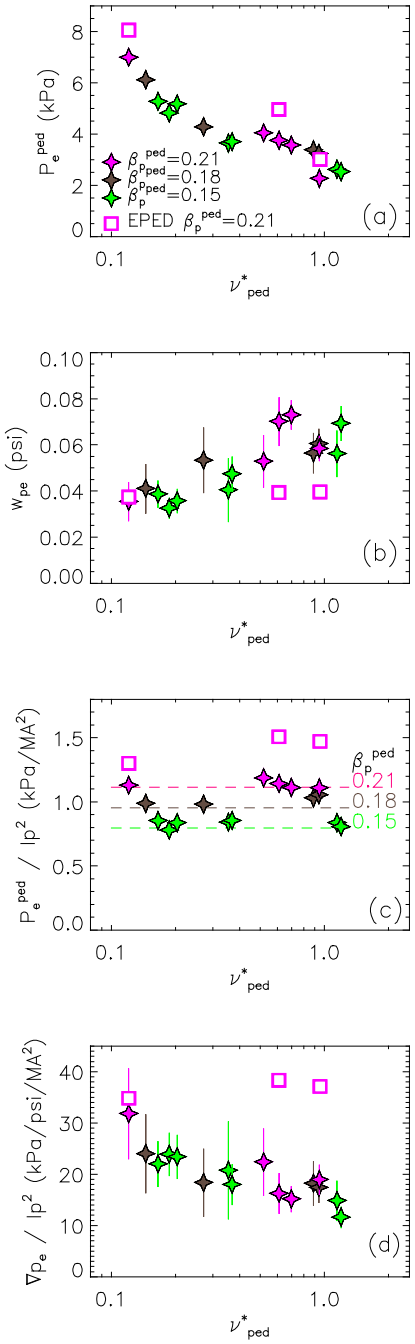

Figure 12. *Electron Pedestal pressure height (a) and width (b) versus pedestal collisionality. Pressure height normalized to plasma current (c) and gradient normalized to plasma current (d) versus pedestal collisionality. Experimental data are shown with full stars and EPED1 predictions with empty squares.*

Despite the fact that EPED1 predicts no significant difference in the pedestal stability, the predicted pedestal pressure has a clear increase with decreasing collisionality (figure 12a). In fact, constant α_{max} does not automatically imply constant pedestal pressure. α_{max} is proportional to the pressure gradient and inversely proportional to the plasma current via the second derivative in ψ [see equation (11)]: $\alpha_{max} \propto p'/I_p^2$. Basically, with the same pedestal stability, higher plasma current can sustain higher pedestal pressure. In the present dataset, the plasma current is increased at low collisionality in order to maintain ρ^* constant, as shown in figure 2(b). Once the I_p^2 dependence is removed, the EPED1 pedestal pressure has no correlation with the collisionality, as shown in figure 12(c).

Figure 12(c) shows the pedestal pressure height normalized to the plasma current also for the experimental data. Since the dataset has been selected to have constant β_p^{ped}, it is obvious that the experimental data show no trend of p_e^{ped}/I_p^2 versus collisionality. However, this does not imply that the experimental data show no change in the pedestal stability and does not imply that the increase of the pedestal height with decreasing collisionality is due only to the increase in the plasma current. In fact, since the pedestal width is reduced at low collisionality, the experimental pressure gradient normalized to Ip^2 increases with decreasing collisionality, as shown in figure 12(d). The

EPED1 predicted pressure gradient normalized to Ip^2 shows instead no trend with collisionality because the EPED1 pedestal width is constant.

In conclusion, while the experimental data show an improvement of the pedestal stability at low ν*, the EPED1 predicts no difference in the pedestal stability with collisionality.

6. STABILITY ANALYSIS.

The pedestal stability of the experimental plasmas has been studied using ELITE to obtain the *j*-α stability diagram and the self-consistent path in the *j*-α space. Here *j* is the current density and α the normalized pedestal pressure gradient, as defined earlier. The equilibrium has been calculated using the HELENA code [Huysmans CP1991]. It uses as input the fit to the experimental T_e and n_e profiles selected in the pre-ELM phase. The profiles are shifted accordingly to a two-point model for the power balance at the LCFS [Kallenbach JNM2005] in order to determine the separatrix electron temperature T_e^{sep}. The edge bootstrap currents are calculated using the Koh-model [Koh PoP2012] which at high collisionality gives a more reliable result (i.e. closer to the results obtained with the drift kinetic code NEO [Belli PPCF2012, Belli PPCF2014]) than with the more common approach described in [Sauter PoP 1999].

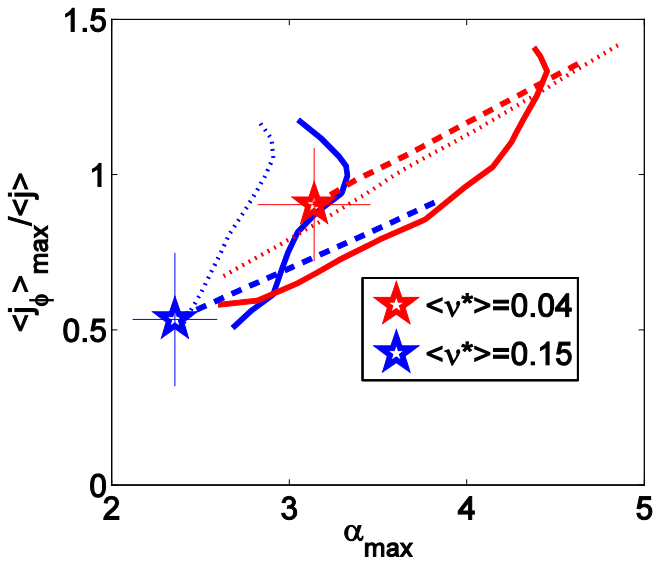

Figure 13. *j-α stability diagram for low (red) and high (blue) collisionality plasmas with $\beta_p^{ped} \approx 0.21$. The stars show the operational point. The continuous lines show the stability boundary calculated with n up to 70. The thin dashed lines show the n=∞ boundary. The thick dashed lines show the self-consistent path in the stability diagram.*

To determine the stability boundary, two approaches have been used. (I) The normalized pressure gradient and the current density have been perturbed from the experimental values in order to obtain the *j*-α diagram with the stability boundary. This approach is useful to investigate the location of the operational point (i.e. the experimental *j* and α) in relation to the boundary. (II) The height of the pedestal temperature is varied and the current profile is calculated self-consistently to find the marginally stable pedestal temperature height. This approach allows estimating the self-consistent path in the *j*-α diagram starting from the operational point till the stability limit is reached and allows quantifying the α_{max} expected from the point of view of the peeling-ballooning stability model. In the stability calculation the modes up to *n=70* have been considered.

The results for a low and high collisionality case with same pedestal beta ($\beta_p^{ped} \approx 0.21$) are shown in figure 13. In both cases, the operational points are in the stable region, far from the *n=70* boundary (thick continuous line). This disagreement in not understood yet. It cannot be

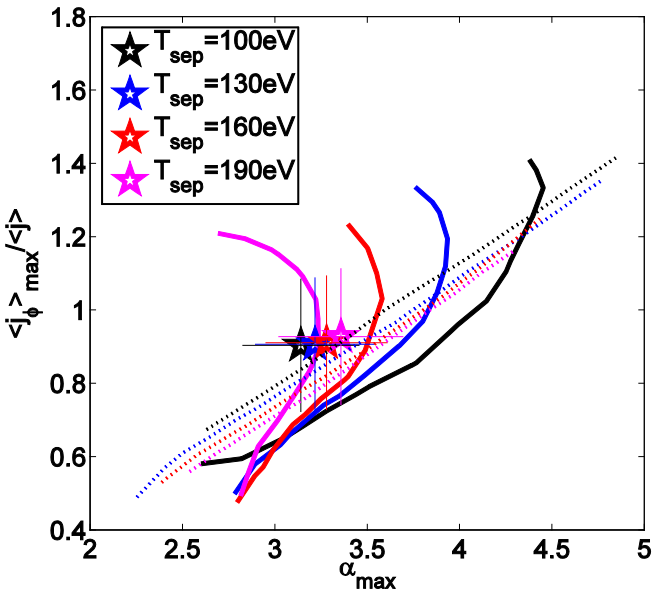

Figure 14. *j-α stability diagram for a low collisionality plasma ($\nu^*_{ped}\approx 0.01$) with $\beta_p^{ped}\approx 0.21$ shifting the experimental profiles in order to obtain a different separatrix temperature. The stars show the operational point. The continuous lines show the stability boundary calculated with up to n=70. The thin dashed lines show the n=∞ boundary.*

ascribed to the stability criterion used ($\gamma>0.03\omega_A$ is used in the present work) as discussed [Maggi NF2015]. The disagreement is, however, consistent with the earlier stability analysis in JET-ILW [Beurskens NF2014, Leyland NF2015, Maggi NF2015]. In particular, the results described in [Maggi NF2015] in low-δ JET-ILW plasmas at I_p=1.4MA B_T=1.7T and $\nu^*_{ped}\approx$0.3-3 show that the operational point is near the *n=70* boundary at low D_2 gas injection ($\Gamma_{D2}\approx 0.3\cdot10^{22}$ e/s) while it is in the stable region at higher gas ($\Gamma_{D2}>0.8\cdot10^{22}$ e/s). The present plasmas have $\Gamma_{D2}>10^{22}$ (e/s) a value comparable to the high gas plasma in [Maggi NF2015].

A source of discrepancy between the operational point and the stability boundary might be that the present modelling does not consider kinetic effects such as those related to the ion diamagnetic drift. These kinetic effects might affect the stability of an ideal ballooning mode [Hastie PoP2003] and further influence the stability boundary [Aiba NF2012].

A further point to discuss is the uncertainty related to the experimental profile position. As earlier described, before performing the stability analysis, the profiles are shifted accordingly to a two-point model in order to have T_e^{sep}=100eV. In principle, small variations in T_e^{sep} might produce relevant changes in the stability boundary. To test the sensitivity of the stability boundary on T_e^{sep}, the stability analysis has been repeated by shifting the profiles in order to vary T_e^{sep} in the range 100-190eV. The results are summarized in figure 14 for the low ν* case. The operational point is on the *n=70* stability boundary at $T_e^{sep}\approx$160eV. This value seems unrealistically too high to conclude that the uncertainty in the experimental profile position is the cause of the fact that the operational point is in the stable region.

Finally, it is necessary to highlight that for an accurate estimation of the boundary position it might not be sufficient to consider only the modes up to *n=70*. So, in figure 13 the *n=∞* boundary is shown with the thin dashed lines. In this case, the operational point is located on *n=∞* boundary.

In conclusion, the stability analysis shows a good agreement with the experimental results when considering the $n=\infty$ boundary. When considering the *n=70* boundary, no quantitative agreement is observed, however, a reasonable qualitative agreement is present. In fact, the *n=70* boundary reaches higher normalized pressure at low ν* than at high ν*. Basically, the stability analysis suggests an improvement of the pedestal stability both considering the $n=\infty$ boundary and the *n=70* boundary.

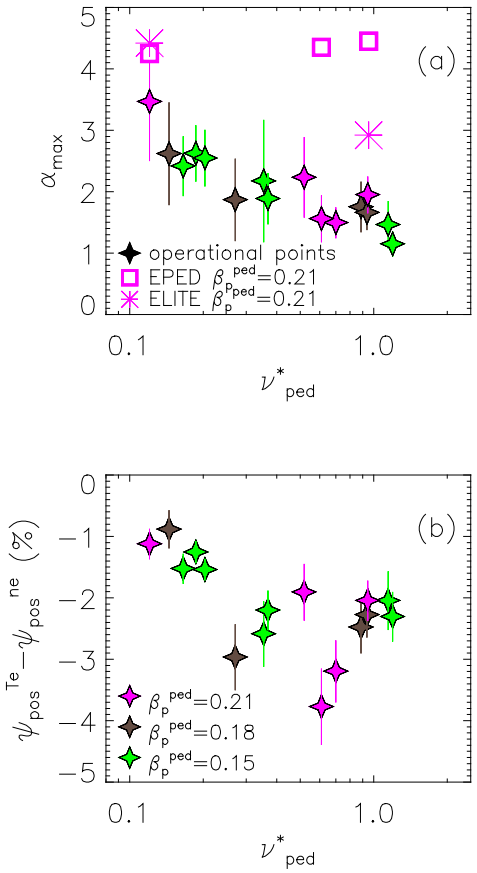

Figure 15. *(a) α_{max} versus collisionality. Asterisks show the results of the P-B stability analysis, squares show the EPED1 value and the full symbols show the operational points for the experimental dataset. (b) Difference between T_e and n_e pedestal position versus collisionality. A more negative value implies a n_e profile shifted more outwards.*

This can be quantified for the *n=70* boundary by calculating the self-consistent path of the operational points. The thick dashed lines in figure 13 show the self-consistent path from the operational points till the corresponding *n=70* boundary. The intersection of the self-consistent path with the *n=70* boundary is used to determine the normalized pressure gradient expected by the stability analysis, α_{max}. The corresponding α_{max} versus collisionality are shown in figure 15(a) (pink asterisks). A clear reduction of α_{max} with increasing ν* is present. For comparison, figure 15(a) shows also the normalized pressure gradient corresponding to the operational points of the experimental dataset (full symbols). A reduction of α with increasing collisionality is observed as well. Basically, both the experimental data and the stability analysis show that the pedestal stability improves with decreasing collisionality.

The increase of α_{max} at low collisionality (i.e. the pedestal stability improvement) is due to at least two factors. (1) The pedestal is narrower at low collisionality than at high collisionality. The reduction of the width has a stabilizing effect on the pedestal [Snyder NF2011]. (2) The position of the density pedestal is more inward at low collisionality than at high collisionality, while the position of the temperature pedestal does not change significantly, see figure 15(b). This is also shown in the profiles in figure 9. The reduction in the relative shift between n_e and T_e pedestal position with decreasing ν* has a stabilizing effect on the pedestal [Beurskens PPCF2009]. A further third factor, that in the present dataset seems to have only a minor

effect, might be the increases the slope of the self-consistent path in the j-α diagram with decreasing collisionality. The first two effects improve the stability at low collisionality and move the boundary to higher α_{max}. Then, the third effect tend to move the intersection of the boundary with the self-consistent path to further higher α_{max}.

7. ELECTRON DENSITY IN THE SCRAPE-OFF LAYER

The collisionality scan affects not only the pedestal density height and width, but also the scrape-off layer (SOL) density. Figure 16(a) shows the density profile for the high collisionality shot of the present dataset that shows the highest SOL density. In this case, the assumption $n_e^{SOL}=0$ used in equation (5) to fit the experimental data is not optimal. No significant difference is observed in the SOL temperature within the experimental HRTS uncertainty (no better diagnostic is available for the measurement of the SOL temperature). The SOL temperature is not further discussed.

The *mtanh* function discussed in equation (5) cannot properly describe the density shape outside the separatrix for the highest collisionality shots. The standard *mtanh* function can be adapted in several ways to better fit the SOL density. The HRTS diagnostic shows a decrease of the SOL density moving outwards from the separatrix. This observation has been confirmed with the reflectometer and the Li-beam. So, a valid alternative for the density fits is to add a SOL slope to equation (5):

$$mtanh^{SOL}(r)=\frac{h}{2}\left(\frac{\left(1+s^{core}x\right)e^{x}-\left(1+s^{SOL}\right)e^{-x}}{e^{x}+e^{-x}}+1\right) \tag{12}$$

The comparison of the fits using equation (5) and equation (12) is shown in figure 15(a). The fit using equation (12) better reproduces the SOL density profile.

However, the SOL density has no direct impact on the result related to the stability analysis and to the pedestal width. Figure 16(b) shows the pressure gradient calculated using the two fitting functions and no difference is observed. This is because the temperature is close to zero in the SOL, so the pressure is not significantly affected by a non-zero SOL density. Since no measurable difference is observed in the pressure gradient, no difference is expected in the stability analysis using the $mtanh^{SOL}$ function. However, we must highlight that this conclusion applies to present plasmas, while in other machines or in other experimental scenarios, where the density pedestal might be more inward [Wolfrum EPS2015], a direct effect of the SOL density on the pressure gradient is possible.

The use of equation (12) can affect also the density width estimation. In fact, the bottom of the pedestal is slightly more inward with $mtanh^{SOL}$ than with the standard *mtanh*, see the vertical dashed lines in figure 16(a). The correlation of the density width with the pedestal collisionality is shown in figure 16(c) using the standard *mtanh* (full symbols) and $mtanh^{SOL}$ (empty symbols). In general, the width estimation with $mtanh^{SOL}$ tends to be slightly narrower

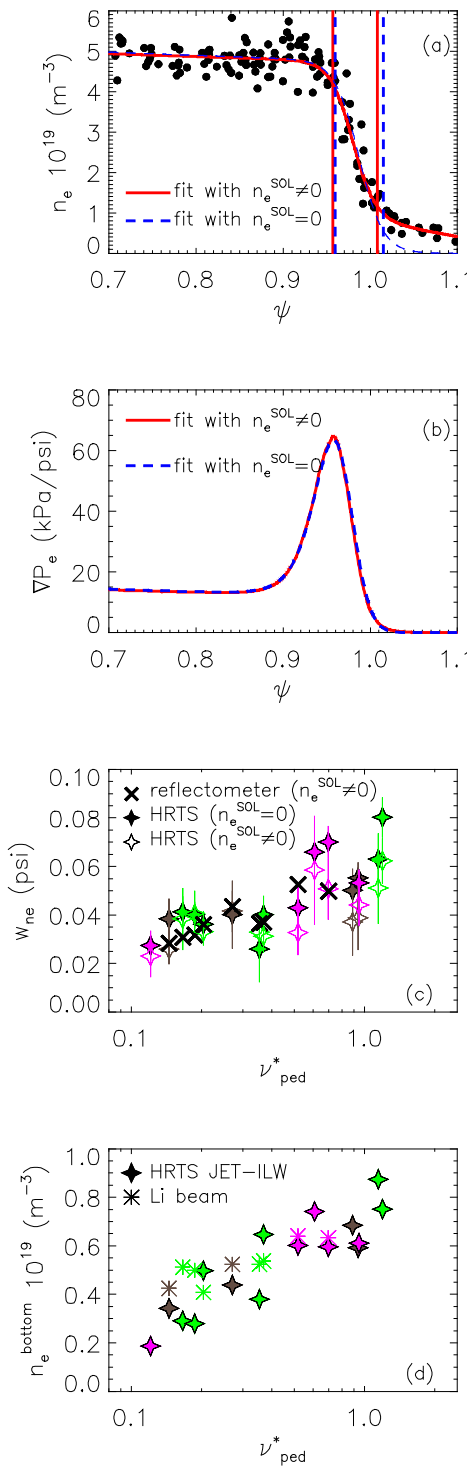

Figure 16. *(a) electron density profile for a high ν* shot (87265) with the fit using mtanh and mtanh^{sol}. The vertical lines highlight the pedestal width. (b) Corresponding pressure gradient. Density width estimated with standard mtanh and mtanh^{sol} (c) density at the bottom of the pedestal (d) versus collisionality.*

than the estimation with the standard *mtanh*. However, the positive trend with collisionality is still present and within the experimental uncertainty no major difference is observed.

The density width determined with the HRTS has been compared with that determined from the reflectometer. The reflectometer data have been fitted using the $mtanh^{SOL}$ function. When the reflectometer data were available, a reasonable agreement with the HRTS has been observed [see the crosses in figure 16(c)].

The correlation between the density estimated at the pedestal bottom (n_e^{bottom}) versus the pedestal collisionality is shown in figure 16(d). Since the HRTS has not an optimal spatial resolution in the SOL region, the estimation of n_e^{bottom} from the HRTS has been compared with the Li-beam, when available. In this dataset, the Li-beam can cover only the SOL and part of the pedestal region, so it cannot be used to estimate the pedestal width. Figure 16(d) shows a clear increase in n_e^{bottom} with collisionality. As discussed in figure 16(b), this behaviour does not have a direct measureable impact on the pressure gradient. However, we can speculate that the high n_e^{bottom} at high collisionality might cool down the SOL reducing the SOL temperature. These combined effects might increase the SOL collisionality and consequently affect the bootstrap current at the separatrix which, in turn, might affect the pedestal stability. So, we cannot exclude that the

reduction of the pedestal stability with increasing collisionality is also related to the increase in SOL density. Due to the lack of good experimental temperature measurements in the SOL, further claims are not possible. Further investigations might rely on a detailed modelling work, for example as recently done for the N_2 seeding plasma [Saarelma PoP2015] using the EDGE2D-EIRENE code [Reiter JNM1992, Simonini CPP1994].

8. CONSLUSIONS.

This work shows that in JET-ILW a strong correlation between the confinement and the collisionality is present. While at high collisionality the confinement is low, with $H_{98}\approx0.8$, at low collisionality JET-ILW can reach high confinement, with $H_{98}\approx1.0$, comparable to JET-C.

The increase of confinement at low collisionality is driven both by the increase in the core and in the pedestal pressure. At the pedestal, the reduction of the density is compensated by a stronger increase of the temperature, which leads to an increased pressure. In the core, the increased pressure is due to two factors: (i) the increase of T_e^{ped} leads to the increase of T_e^{core} via the T_e profile stiffness, and (ii) the reduced collisionality leads to higher density peaking and higher pressure peaking further increasing the role of the core respect to the pedestal.

The strong increase of the pedestal with the decreasing collisionality is due to two factors.

(1) The increase of the plasma current at low collisionality. Assuming similar pedestal stability, the higher plasma current at low collisionality can sustain a higher pedestal gradient.

(2) The improvement of the pedestal stability. This has been observed experimentally via the increase of the pedestal pressure gradient normalized to Ip^2 with the decreasing ν^*. A qualitative agreement with the P-B stability has been observed.

The pedestal stability improvement at low collisionality is related to at least two factors: (i) the reduction of the pedestal width at low ν^*, (ii) the lower relative shift between density and temperature pedestal position. The steeper self-consistent path in the stability diagram might be a possible third cause.

A significant change in the pedestal structure has been observed. In particular the pedestal width narrows with decreasing collisionality. The reason for the pedestal width scaling with collisionality is still unclear and this behaviour is not well reproduced by the KBM constraint. This suggests that the present models for the pedestal width estimation might be not sufficient to describe in detail the pedestal behaviour. Nonetheless, at low collisionality a good agreement has been observed between the KBM constraint and the experimental data. Moreover, an extrapolation to low ν^* suggests that the KBM pedestal width predictions are reasonable at ITER-relevant collisionality.

From the point of view of the pedestal height, the EPED1 results show a trend with collisionality that is qualitative similar to the experimental data. However, the EPED1 trend is due only to the higher plasma current used in the low ν^* shots and no significant changes in the EPED1 pedestal stability are observed. At low collisionality, where the EPED1 pedestal width is consistent with the experimental results, the EPED1 predicted pedestal stability is in

agreement with the α_{max} determined with the P-B stability analysis. At high collisionality, the EPED1 predicted α_{max} is significantly higher than the α_{max} determined from the P-B stability. At high collisionality, EPED1 can still predict reasonably well the pedestal pressure height because its overestimated α_{max} is compensated by the underestimated pedestal pressure width.

The experimental results suggest that the SOL might play a role in the pedestal stability. Including the effects in the SOL might be necessary to reach a more reliable description of the pedestal physics. Further investigations on this point are necessary.

ACKNOWLEDGEMENT

This work has been carried out within the framework of the EUROfusion Consortium and has received funding from the Euratom research and training programme 2014-2018 under grant agreement No 633053. The views and opinions expressed herein do not necessarily reflect those of the European Commission.

REFERENCES

[Aiba NF2012] Aiba N and Oyama N, *Nucl. Fusion* **52** 114002 (2012)
[Angioni PoP 2009] Angioni C. *et al., Phys. Plasmas* **16** 060702 (2009)
[Angioni PRL 2003] Angioni C., et al., *Phys. Rev. Lett.* **90** 205003 (2003)
[Belli PPCF2012] Belli E. *et al., Plasma Phys. Control. Fusion* **54** 015015 (2012)
[Belli PPCF2014] Belli E. *et al., Plasma Phys. Control. Fusion* **56** 045006 (2014)
[Beurskens PPCF2009] M.N.A. Beursknes *et al., Plasma Phys. Control. Fusion* **51** 124051 (2009)
[Beurskens PoP2011] M.N.A. Beursknes *et al., Phys. Plasmas* **18** 056120 (2011)
[Beurskens NF2013] M. Beurskens et al., *Nucl. Fusion* **53** 013001 (2013)
[Beurskens NF2014] M. Beurskens et al., *Nucl. Fusion* **54** 043001 (2014)
[Bourdelle NF2011] C. Bourdelle, Nucl. Fusion **51** 063037 (2011)
[Brezinsek IAEA2012] S. Brezinszek et al., "24th IAEA Fusion Energy Conference", San Diego, USA, 2012, pp EX/4-1.
[Challis NF2015] C. Challis et al., *Nucl. Fusion* **55** 053031 (2015)
[Cordey EPS2004] Cordey J G *et al* 2004 *Proc. 31st EPS Conf. on Plasma Physics (London, UK)* vol 28G (ECA) O1.05
[Frassinetti NF2015] L. Frassinetti *et al., Nucl. Fusion* **55** 023007 (2015)
[Frassinetti RSI 2012] L. Frassinetti, et al., *Rev. Sci. Instrum.* 83, 013506 (2012)
[Giroud NF2013] C. Giroud et al., *Nucl. Fusion* **53** 113025 (2013)
[Giroud PPCF 2015] C. Giroud et al., *Plasma Phys. Control. Fusion* **57** 035004 (2015)
[Greenwald NF2006] Greenwald M. et al, *Nucl. Fusion* **47** L26 (2007)
[Groebner NF2001] R.J. Groebner *et al., Nucl. Fusion* **41** 1789 (2001)
[Groebner NF2004] R.J. Groebner *et al., Nucl. Fusion* **44** 204 (2004)
[Groebner NF2013] R.J. Groebner *et al., Nucl. Fusion* **53** 093024 (2013)
[Hastie PoP2003] Hastie R.J., Ramos J.J. and Porcelli F. *Phys. Plasmas* **10** 4405 (2003)
[Huysmans CP1991] Huysmans G.T.A. *et al, Computational Physics: Proc.Int. Conf. (Amsterdam, The Netherlands, 1991) (Singapore: World Scientific)*
[Huysmans PPCF 2005] Huysmans G.T.A. *et al., Plasma Phys. Control. Fusion* **47** B165 (2005)
[Joffrin IAEA 2014] E. Joffrin et al., *Proc. 25th Int. Conf. on Fusion Energy (Saint Petersburg, 2014)* EX/P5-40 http://www-pub.iaea.org/iaeameetings/46091/25th-Fusion-Energy-Conference-FEC-2014
[Kadomstev SJP1975] Kadomstev B B *Sov. J. Plasma Phys.* **1** 295 (1975)

[Kallenbach JNM2005] A. Kallenbach *et al., J. of Nucl. Mater.* **337-339** 381 (2005)
[Kaye NF2013] S.M. Kaye et al., *Nucl. Fusion* **53** 063005 (2013)
[Kho PoP2012] S. Kho et al., *Phys. Plasmas* **19**, 072505 (2012);
[Kinsey NF2011] Kinsey J.E. *et al., Nucl. Fusion* **51** 083001 (2011)
[Kirk PPCF2004] A. Kirk *et al., Plasma Phys. Control. Fusion* **46** A187 (2004)
[Konz EPS2011] Konz C. *et al EPS Conf. on Plasma Physics* (Strasbourg, France, 2011) O2.10 (2011)
[Leyland NF2013] M. Leyland *et al., Nucl. Fusion* **53** 083028 (2013)
[Leyland NF2015] M. Leyland *et al., Nucl. Fusion* **55** 013019 (2015)
[Loarte, PPCF 2003] Loarte et al., *Plasma Phys. Control. Fusion* **45** 1549 (2003)
[Lomas EPS2015] P. Lomas et al., *42th EPS Conf. on Plasma Physics*, Lisbon, Portugal (2015)
[Luce PPCF2008] T.C. Luce, C.C. Petty and J.C. Cordey, *Plasma Phys. Control. Fusion* **5**0, 043001 (2008)
[de la Luna IAEA2014] E. de la Luna et al. *Proc. 25th Int. Conf. on Fusion Energy (Saint Petersburg, 2014)* EX/P5-195 http://www-pub.iaea.org/iaeameetings/46091/25th-Fusion-Energy-Conference-FEC-2014
[de Vries NF2008] de Vries P.C. *et al Nucl. Fusion* **48** 065006 (2008)
[Mc Donald IAEA2004] McDonald D C *et al* 2004 *20th IAEA Fusion Energy Conf. (Vilamoura, Portugal)* EX6-6
[Maggi NF2015] C. Maggi et al., submitted to *Nucl. Fusion*
[Maggi NF2010] C. Maggi *et al., Nucl. Fusion* **50** 025023 (2010)
[Mahdavi PoP2003] Mahdavi M.A.et al., *Phys. Plasmas* **10** 3984 (2003)
[Maslov NF2009] M. Maslov et al., Nucl. Fusion **49** 075037 (2009)
[Matthews 2012] G. Matthews et al., J. Nucl. Mat. 438, S2 (2013)
[Mikhailovskii PPR1997] A.B. Mikhailovskii *et al., Plasma Phys. Rep.* **23** 844 (1997)
[Miller PoP1998] Miller R.L. *Phys. Plasmas* **5** 973 (1998)
[Nunes IAEA2014] I. Nunes et al., 25th IAEA Fusion Energy Conf. (S. Petersburg, 2014) EX/9-2
[Nunes EPS2014] I. Nunes et al., *42th EPS Conf. on Plasma Physics*, Lisbon, Portugal (2015) O1.001
[Onjun PoP2002] Onjun T. *et al*., *Phys. Plasmas* **9** 5018 (2002)
[Petty, PoP1999] C.C Petty and T.C Luce, *Phys. Plasmas* **6** 909 (1999)
[Pasqualotto RSI 2004] R. Pasqualotto, P. Nielsen, C. Gowers *et al., Rev. Sci. Instrum.* **75**, 3891 (2004).
[Reiter JNM1992] Reiter D., *J. of Nucl. Mater.* **88** 196 (1992)
[Saarelma PPCF 2009] Saarelma S. *et al., Plasma Phys. Control. Fusion* **51** 035001 (2009)
[Saarelma NF 2013] Saarelma S. *et al., Nucl Fusion* **53** 123012 (2013)
[Saarelma PoP 2015] Saarelma S. *et al., Phys. Plasmas* **22** 056115 (2015)
[Saibene PPCF2002] G. Saibene *et al., Plasma Phys. Control. Fusion* **44** 1769 (2002)
[Sauter PoP1999] Sauter O. and Angioni C. *Phys. Plasmas* **6** 2834 (1999)
[Schneider PPCF2015] Schneider P.A. *et al., Plasma Phys. Control. Fusion* **57** 014029 (2015)
[Schweinzer NF2011] Schweinzer J. *et al.,Nucl. Fusion* **51** 113003 (2011)
[Simonini CPP1994] Simonini R. *et al., Contributions to Plasma Physics* **34** 368 (1994)
[Sirinelli RSI 2010] A. Sirinelli, B. Alper, C. Bottereau, et al., *Rev. Sci. Instrum*. 81, 10D939 (2010)
[Shimada NF2007] Shimada et al., *Nucl. Fusion* **47**, S1 (2007)
[Snyder PoP2002] Snyder P.B. *et al., Phys. Plasmas* **9** 2037 (2002)
[Snyder PoP2009] P.B. Snyder *et al., Phys. Plasmas* **16** 056118 (2009)
[Snyder NF2011] P.B. Snyder *et al., Nucl. Fusion* **51** 103016 (2011)
[Takenaga NF2008] Takenaga H. *et al., Nucl. Fusion* **48** 075004 (2008)
[Urano NF2008] H. Urano *et al., Nucl. Fusion* **48** 103016 (2008)
[Urano NF2014] H. Urano *et al., Nucl. Fusion* **54** 116001 (2014)
[Urano EPS2015] H. Urano et al., *42th EPS Conf. on Plasma Physics*, Lisbon, Portugal (2015) P5.146
[Urano NF2015] H. Urano *et al.,accepted in Nucl. Fusion* (2015)
[Valovic PPCF2004] Valovic M. *et al., Plasma Phys. Control. Fusion* **46** (2004)
[Weisen PPCF2006] Weisen H. *et al., Plasma Phys. Control. Fusion **48** A457 (2006)*
[Wilson PoP2002] Wilson H.R. *et al., Phys. Plasmas* **9** 1277 (2002)
[Wolfrum NF2015] Wolfrum E. *et al., Nucl. Fusion* **55** 053017 (2014)
[Wolfrum EPS2015] Wolfrum E. *et al., 42th EPS Conf. on Plasma Physics*, Lisbon, Portugal (2015) P1.115
[Verdoolaege Entropy2015] Verdoolaege G., *Entropy* **17**, 4602 (2015).